Nuclear Engineering and Technology 54 (2022) 2614–2624

Contents lists available at ScienceDirect

Nuclear Engineering and Technology

journal homepage: www.elsevier.com/locate/net

Original Article

Comparative optimization of $Be/Zr(BH_4)_4$ and $Be/Be(BH_4)_2$ as ^{252}Cf source shielding assemblies: Effect on landmine detection by neutron backscattering technique

Nassreldeen A.A. Elsheikh

Al-Baha University, College of Science & Arts, Al-Mikhwah, Department of Physics, P.O. Box 1988, Al-Baha, Saudi Arabia

ARTICLE INFO

Article history:
Received 5 October 2021
Received in revised form
8 January 2022
Accepted 24 January 2022
Available online 27 January 2022

Keywords:
Monte Carlo simulations
Neutron backscattering
Landmine detection
Metal borohydrides
^{252}Cf neutron source

ABSTRACT

Monte Carlo simulations were used to model a portable Neutron backscattering (NBT) sensor suitable for detecting plastic anti-personnel mines (APMs) buried in dry and moist soils. The model consists of a 100 MBq ^{252}Cf source encapsulated in a neutron reflector/shield assembly and centered between two ^{3}He detectors. Multi-parameter optimization was performed to investigate the efficiency of $Be/Zr(BH_4)_4$ and $Be/Be(BH_4)_2$ assemblies in terms of increasing the signal-to-background (S/B) ratio and reducing the total dose equivalent rate. The MCNP results showed that 2 cm Be/3 cm $Zr(BH_4)_4$ and 2 cm Be/3 cm $Be(BH_4)_2$ are the optimal configurations. However, due to portability requirements and abundance of Be, the ^{252}Cf-2 cm Be/3 cm $Be(BH_4)_2$ NBT model was selected to scan the center of APM buried 3 cm deep in dry and moist soils. The selected NBT model has positively identified the APM with a S/B ratio of 886 for dry soils of 1 wt% hydrogen content and with S/B ratios of 615, 398, 86, and 12 for the moist soils containing 4, 6, 10, and 14 wt% hydrogen, respectively. The total dose equivalent rate reached 0.0031 mSv/h, suggesting a work load of 8 h/day for 806 days within the permissible annual dose limit of 20 mSv.

1. Introduction

Landmine detection is one of the most beneficial applications of nuclear techniques that address the concerns of public safety authorities in nearly 70 countries around the world, which are affected by more than 80 million landmines that kill or maim about 2000 people every month [1]. Among the nuclear techniques that have been successfully used to identify landmines is Pulsed Elemental Analysis with Neutrons (PELAN) [2]. Like other neutron-based techniques, PELAN relies on the fact that most explosives used in landmines: TNT ($C_7H_5N_3O_6$), RDX ($C_3H_6N_6O_6$) or hexogen ($O_8N_8C_4H_8$) are mainly composed of four basic elements: Hydrogen, Carbon, Nitrogen, and Oxygen [3,4]. These elements differ significantly in the way they interact with neutrons, which allows the determination of the nature and concentration of a particular element by fast and/or thermal neutron activation analysis.

In this technique, a pulsed 14 MeV (d-T) neutron generator is used to excite C and O nuclides by $^{12}C(n,n'\gamma)\,^{12}C$ and $^{16}O(n,p)^{16}N$ reactions and detect the resulting characteristic γ-lines at 4.44 MeV and 6.13 MeV, respectively [5,6]. When the pulse is stopped, the fast neutrons lose their energy due to collisions with the light elements in the soil and can be slowed to a sufficiently low neutron energy (<1 MeV), which depends primarily on the hydrogen concentration in the soil. In this energy range, hydrogen and nitrogen in the landmine can be activated by thermal neutron capture reactions $^{1}H(n,\gamma)^{2}H$ and $^{14}N(n,\gamma)^{15}N$, releasing the characteristic 2.223 MeV γ-line for hydrogen and 10.83 MeV γ-line for nitrogen [6,7]. The landmine detection problem is thus reduced to an elemental characterization problem. The released γ-ray energies identify the neutron-capturing elements, while the intensities of the peaks at these energies reveal their concentrations [8].

However, in addition to the complexity associated with the analysis before and after pulse activation, the hydrogen content in the soil also depends on its moisture content. Consequently, in soils with low water content, the flux density of thermalized neutrons impinging on the buried anomaly may be too low to allow unambiguous post-pulse activation analysis [9]. On the other hand, one of the major limitations to the use of such sensors is their heavy weight (<45 Kg for PELAN) [2] and their size which makes them useable only in vehicle-mounted systems.

An alternative, simpler nuclear method for detecting non-metallic landmines that has shown great potential for developing hand-held systems is the neutron backscattering technique (NBT) [10–16]. The motivation for this technique is the significant amount of hydrogen in landmine explosives, estimated at (25–30) atom% [4].

E-mail address: nassreldeen.elsheikh@yahoo.com.

https://doi.org/10.1016/j.net.2022.01.029

Consequently, anti-personnel mines (APMs) buried in dry soils represent significant hydrogen rich anomalies. At neutron energies below about 3 MeV, the total cross section of the (n,p) reaction on ^{1}H is much higher than that of other nuclides commonly found in soil. Combined with this fact, the elastic $^{1}H(n,n)^{1}H$ scattering, which is the dominant process in the (n,p) reactions on ^{1}H at these energies, has an average energy loss of (50%) per elastic collision with a neutron. This fact makes hydrogen nuclei in the explosive material of much higher ability to moderate neutron energy than heavier soil elements. Furthermore, measurements in the laboratory have shown that the scattering angle of the neutron cannot exceed 90° [17].

Based on such considerations, NBT uses an isotopic neutron source with average energy (<3 MeV) such as ^{252}Cf and a thermal neutron detector with high efficiency such as a ^{3}He proportional counter [3,18]. Both ^{252}Cf and ^{3}He are coupled in a suitable geometry and placed above the soil. The fast neutrons from the ^{252}Cf source are moderated in both the landmine and the surrounding soil and scattered back to the ^{3}He detector. However, due to the higher hydrogen content in the landmine, an increase in the number of backscattered thermal neutrons is achieved above the location where the mine is buried [2]. Therefore, to confirm the presence of the mine, a NBT sensor checks for the presence of a hydrogenous anomaly in the target volume [3]. The amount of detected thermal neutrons without landmine (I_o) is subtracted from the moderated neutrons in the soil with buried landmine (I). In this way, a net signal ($I-I_o$) from the landmine is produced, which is then used to determine the signal-to-background ratio [$S/B=(I-I_o)/I_o$].

Further improvements were achieved by using two identical ^{3}He detectors placed at a certain distance from each other, with the ^{252}Cf source placed exactly in the middle [12,13]. This was proposed to reduce the sensitivity of the signal from a NBT device with a single neutron detector for variations in detector position. When the landmine is scanned with such NBT geometry, the detector above the landmine will count a higher thermalized neutron flux than the detector above the soil. When both signals are subtracted, a reference value is available and the dependence on detector position is reduced [12]. In this context, Brooks and Drosg (2005) [19] used the difference between the count rates of two identical BF_3 detectors to generate a wave-like deflection signature indicating the presence of a hydrogen-rich anomaly, possibly a landmine.

However, soil may contain different concentrations of hydrogen depending on its moisture content. A specific analysis of this problem [20] concluded that the critical value of soil moisture, reached when the density of hydrogen atoms in the landmine is equal to that of the background soil, defines a condition ($I-I_o \leq 0$) at which detection is not possible. Therefore, the NBT method is best used in countries where soil moisture is generally below 10%, a condition that applies to dry soils.

This fact raises the challenge of optimizing NBT geometries capable of detecting buried landmines with a sufficient S/B ratio in both dry and moist soils. To achieve this, the neutron flux density from the source towards the mine-contaminated soil should be maximized by the proper selection of a neutron reflector. On the other hand, for hand-held NBT systems, unlike vehicle-mounted systems, the radiation protection requirements for the human user take precedence over finding effective shielding to reduce the dose to the lowest reasonably achievable level.

In this work, such a possibility is explored by modeling a cylindrical reflector/shield unit that encapsulates a ^{252}Cf source located midway between two identical ^{3}He detectors. The choice of the (^{3}He-^{252}Cf-^{3}He) geometry for the current NBT model was motivated by the excellent results of laboratory measurements and Monte Carlo simulations reported for NBT prototype devices with a similar geometry (detector-source-detector) [14,17,19]. These results have confirmed the feasibility of such NBT devices that are easy to use, light enough to be man-portable, and nondestructive.

A suitable reflector must have a low absorption cross section and a high elastic scattering cross section to direct neutrons to the desired region [21]. Among the various fast neutron reflectors, graphite (C) and beryllium (Be) are widely used for ^{252}Cf-based nondestructive detection geometries and have been shown to reflect fast neutrons effectively [8,22]. Compared to Be, the thermal neutron capture cross section of ^{12}C (0.0035 b) is about 58% lower than that of ^{9}Be (0.0085 b) [23]. On the other hand, at a neutron energy of 0.7 MeV (the most probable energy of the ^{252}Cf source) [18,24], the elastic scattering cross section of ^{9}Be (3.3965 b) is about 12.5% higher than that of ^{12}C (3.0189 b). Moreover, the neutron multiplication of Be by the ^{9}Be (n,2n) reaction is dominant in the neutron energy range of 1.8–5.9 MeV, which falls within the energy range of the ^{252}Cf source 0.1–6 MeV [24] considered for the current work. In contrast, for the $^{12}C(n,2n)$ reaction, considerable cross sections are observed in the energy range starting from 21 MeV [23]. In addition, the lower density of Be (1.85 g cm^{-3}) compared to that of C (2.23 g cm^{-3}) suggests a lower mass per unit volume of about 17% for Be, which is an additional interesting feature for portable NBT sensors.

Effective neutron shielding should include a moderator with a large scattering cross section, a small absorption cross section, and a large energy loss per collision [8]. In addition, neutron shielding must also include an effective absorber with a high absorption cross section for thermal neutrons. In the search for neutron shielding with such properties, advanced materials such as metal borohydrides are increasingly being used for neutron shielding design [25,26]. This is due to their chemical composition, which is characterized by a higher hydrogen content than in conventional moderators, as well as sufficient boron content. The presence of ^{1}H in a metal borohydride makes it a suitable moderator for fast neutrons, while the presence of boron ^{10}B with its significantly high thermal neutron absorption cross section of 3840 b for the $^{10}B(n,\alpha)^{7}Li$ reaction [27], makes it an effective thermal neutron absorber.

The metal borohydrides such as $Zr(BH_4)_4$ and $Be(BH_4)_2$ contain sufficient hydrogen and boron with atomic number densities of about 7.5×10^{22} atoms.cm^{-3} and 1.9×10^{22} atoms.cm^{-3}, respectively. The presence of the element Zr with high Z number ($Z = 40$) and atomic number density of about 0.5×10^{22} atoms.cm^{-3} in $Zr(BH_4)_4$ may promote direct absorption of γ-rays released by (n,γ) reactions within the shield as well as γ-rays associated with the ^{252}Cf source. The γ-shielding property of Zr is based on the fact that among several photon interactions by which photons dissipate energy, photoelectric absorption (PE) is favored by low energy photons and high atomic number absorbers and is proportional to ($Z^{4.5}/E^{3.5}$) [18,28,29]. Regarding the neutron shielding ability, a specific analysis by Hayashi et al. (2009) [30] concluded that atoms with high Z number such as Zr are effective neutron shielding as well as hydrogen atoms.

On the other hand, the $Be(BH_4)_2$ shield contains the element Be with low Z number and an atomic number density of about 1.5×10^{22} atoms.cm^{-3}. Thus, in addition to ^{1}H, Be can also contribute in thermalizing neutrons enough to be absorbed by ^{10}B via the $^{10}B(n,\alpha)^{7}Li$ reaction, reducing the dose equivalent rate due to neurons. This can compensate for the low gamma shielding due to the absence of high-Z elements in its constituents. In this way, a reasonable total (neutrons and gamma) dose equivalent rate can be achieved. It is worth noting that the density of 0.0604 g cm^{-3} of $Be(BH_4)_2$ compared to 1.18 g cm^{-3} density of $Zr(BH_4)_4$ suggests about 48% lower mass per unit volume for $Be(BH_4)_2$, a property of interest for the geometry of a portable NBT sensor.

In this context, Monte Carlo simulations [31] were performed by Elsheikh (2017) [14] to model a cube-shaped C/$Zr(BH_4)_4$ shielding unit configured to house the entire laboratory-optimized (^{3}He-^{252}Cf-^{3}He) NBT model. Laboratory measurements were performed to develop a (^{3}He-^{252}Cf-^{3}He) NBT device (without shielding) for the detection of plastic APMs buried in dry soils. For this purpose, a^{252}Cf source producing about 0.7×10^4 n.s^{-1} was used, centered between two identical ^{3}He detectors with an effective length of 40 cm and a diameter of 3 cm. The test measurements were performed with an IAEA standard APM (DLM2) of 8 cm diameter and 3.4 cm height buried in a laboratory test bed of dry sand with dimensions 150 cm × 80 cm × 50 cm. The scanning results in terms of S/B ratio demonstrated the applicability of the optimized NBT device for APM detection in dry soils. An optimal S/B ratio of about 32 was achieved when the NBT device crossed the center of the APM in an acquisition time of 1200s.

On the other hand, the MCNP simulations for the effects of the C/$Zr(BH_4)_4$ shielding model were performed in the presence of a^{252}Cf source producing 10^6 n.s^{-1}. The optimal S/B ratio was about 700 for an acquisition time of 100 s. The neutron dose equivalent rate was calculated to be 0.01 mSv/h, suggesting 250 days at a work load of 8 h/day within the permissible annual dose limit of 20 mSv [13]. Compared to the optimal S/B ratio obtained with the laboratory-optimized (^{3}He-^{252}Cf-^{3}He) assembly (32), the proposed C/$Zr(BH_4)_4$ shielding assembly has effectively increased the S/B ratio by a factor of about 21. However, the large size 40 cm × 18 cm × 18 cm of the proposed C/$Zr(BH_4)_4$ configuration and the relatively heavy weight of about 7.8 Kg affect the portability of the proposed NBT device. If, in addition, the gamma dose equivalent rate due to the γ-rays released by (n,γ) reactions originates in the shield and the γ-rays associated with the ^{252}Cf source are included, a higher total dose equivalent rate may result. Consequently, this may result in the need to increase the thickness of the $Zr(BH_4)_4$ shield at the expense of device weight, which should be avoided when developing a portable NBT sensor.

To address such shortcomings, this work proposes a cylindrical reflector/shield Monte Carlo model that instead encapsulates only the ^{252}Cf source. The encapsulated ^{252}Cf source is centered between two identical ^{3}He detectors. Unlike the relatively heavy cube-shaped shielding configuration used in Ref. [14], the current cylindrical ^{252}Cf-reflector/shield capsule reduces the size of the shielding assembly and, depending on the materials selected, may reduce its weight. Comparative optimizations were performed to evaluate the performance of Be/$Zr(BH_4)_4$ and Be/$Be(BH_4)_2$ assemblies in terms of maximizing the S/B ratio due to a buried APM and reducing the total dose equivalent rate to the user.

Several parameters, including the ^{3}He–^{3}He distance, Be-reflector thickness, shielding thickness, stand-off distance (distance between the ^{252}Cf source and the soil surface), APM burial depth, and soil density were comparatively optimized with respect to their effect in identifying a plastic APM buried in dry soils with hydrogen content of 1 wt%. The optimal NBT model based on S/B ratio and total dose rate was determined. However, in terms of portability and abundance of the materials involved, the NBT model with the lower mass and most abundant elements was selected. The applicability of the selected NBT model in dry soils was compared to its applicability in moist soils with hydrogen content in the range of 4–14 wt%. This is done by scanning the selected NBT model across the center of the APM.

Various neutron sources and thermal neutron detectors have been used in a variety of NBT geometric arrangements reported for landmine detection. Isotopic neutron sources such as ^{252}Cf and ^{241}Am–Be and neutron generators such as D-D and D-T generators have been effectively coupled with ^{3}He or BF_3 thermal neutron detectors, resulting in efficient NBT geometries [4,11,14,32].

The neutron source ^{241}Am–Be (α,n) has a half-life of 432.7 years and produces neutrons with an emission rate of 7×10^{-5} n.s^{-1}.Bq^{-1}. The average neutron energy of ^{241}Am–Be is about 4.5 MeV and its neutron energy spectrum covers a range from 2 to 10 MeV [9,33,34]. The spontaneous fission neutron source ^{252}Cf, on the other hand, has a half-life of 2.645 years and emits neutrons at a rate of 1.2×10^{-1} n.s^{-1}.Bq^{-1} [18,33], which is a factor of about 0.17×10^4 higher than that of ^{241}Am–Be. The average neutron energy of ^{252}Cf is about 2.1 MeV, which is lower than that of ^{241}Am–Be by a factor of about 2. The neutron energy spectrum spans an energy range from about 0.1 to 6 MeV [8,24,33]. At this point, it should be noted that the average energy of ^{252}Cf falls within the range of neutron energies desired for the (n,p) reaction on ^{1}H(<3 MeV) [17]. Therefore, for an isotopic neutron source with relatively high neutron flux, low shielding requirements, and average neutron energy suitable for NBT application, it is reasonable to use a^{252}Cf source. Moreover, ^{252}Cf is preferred in this work due to its well-defined energy spectrum and higher specific activity compared to the ^{241}Am–Be source [8].

However, neutron generators based on (D-D) or (D-T) fusion reactions may be a suitable alternative to isotopic neutron sources in reducing the risk of radiation exposure, since they offer the possibility of switching the emitted neutrons on and off [35,36]. This eliminates the need for heavy shielding, which is required for an isotopic neutron source, even when it is not in use.

In addition, D-D and D-T generators emit neutrons at a much higher neutron flux compared to isotopic neutron sources. The fusion reactions ^{2}H(D,n)^{3}He and ^{3}H(D,n)^{4}He produce monoenergetic neutrons with energies of about 2.5 MeV and 14.1 MeV with maximum emission rates of 10^{11} n.s^{-1} and 5×10^{13} n.s^{-1}, respectively [33,36]. Moreover, the use of D-D or D-T generators eliminates the need for waste-disposal, a major problem in the use of isotopic neutron sources [35].

Nevertheless, the operating lifetime of D-D or D-T generators is extremely short compared to the most commonly used isotopic neutron sources ^{252}Cf or ^{241}Am-Be [37]. Consequently, the neutron flux of D-D or D-T neutron generators also decreases as a function of lifetime as the deuterium or tritium atoms on the target degrade [37]. Moreover, D-D and D-T generators are larger than other isotopic neutron sources due to the associated electronics [33]. For this reason, as well as the lack of external power requirements, isotopic neutron sources can be readily incorporated into transportable neutron backscattering units. Based on these considerations, the ^{252}Cf source was selected for the current NBT model where maximum portability is required. In addition, the ^{252}Cf is preferred due to its low cost and low maintenance requirements compared to D-D or D-T neutron generators [33].

Thermal neutron detectors such as ^{3}He and BF_3 are gas-filled proportional counters that have been successfully used in NBT geometries for landmine detection [13,19]. The nuclear reactions for the conversion of thermal neutrons into directly detectable particles in the proportional counters filled with ^{3}He or BF_3 are ^{3}He(n,p)^{3}H and ^{10}B(n,α)^{7}Li, respectively. The ionization produced by the charged particles released in ^{3}He and BF_3 gases triggers the multiplication process that leads to the detection [38]. Both ^{3}He and BF_3 are effective thermal neutron moderators due to their relative stability, efficiency, and insensitivity to gamma-ray photons. However, BF_3 is a highly toxic gas that degrades significantly during use and has a short operational lifetime [38–40]. On the other hand, the use of ^{3}He detectors is limited by the higher operating costs due to the scarcity of ^{3}He [41]. However, the thermal neutron absorption cross section for the ^{3}He(n,p)^{3}H reaction (5330 b) is higher than that of ^{10}B(n,α)^{7}Li (3840 b) by a factor of about 1.4 [38]. This fact provides a higher sensitivity of ^{3}He detectors compared to those of $^{10}BF_3$. For this reason, ^{3}He detectors were selected for our current NBT Monte Carlo model.

2. MCNP modeling

The proposed NBT model was configured in two-dimensional projection and is shown in Fig. 1. The model consists essentially of a point ^{252}Cf source centered on the Y-axis and encapsulated in a cylindrical reflector/shield assembly. The encapsulated ^{252}Cf source was located midway between two identical ^{3}He detectors centered on the Z-axis. Fig. 1 also shows the APM simulant, which was enclosed in a plastic casing and buried in soil. In addition, Fig. 1 shows the x-y plane, with the Z-axis assumed to be perpendicular to the X-axis and Y-axis. The cross sections were taken from the ENDF/B-VI and NJOY libraries. To increase the precision of the results, the MCNP statistical error (R) should be effectively reduced. One way to achieve this is to increase the fraction of histories that hit the ^{3}He detectors. This fraction is increased by increasing the total number of histories (N) using the relationship between R and N determined by the formula [31]:

$$R\alpha 1 \Big/ \sqrt{N} \tag{1}$$

In this work, MCNP calculations were performed with up to 10^7 histories and the acquisition time was increased to 100 s. These choices provided sufficient statistics (fraction of histories that hit the ^{3}He detectors) and resulted in a reasonable error of 0.03%.

2.1. Neutron source

This work uses a point ^{252}Cf source of 100 MBq, producing about 1.15×10^7 n.s^{-1} [13]. The relatively high intensity of the ^{252}Cf source intensity was selected to ensure sufficient neutron flux at the APM location and to maximize the backscattered neutron flux counted by the two ^{3}He detectors. The ^{252}Cf source was centered in a cylindrical air-filled cavity with a diameter of 3 cm and a height of 5 cm, concentrically placed in a cylindrical Be-reflector with a density of 1.85 g cm^{-3} and a varying thickness. The encapsulated ^{252}Cf was located midway and 3 cm below the two ^{3}He detectors.

The neutron energy spectra of ^{252}Cf were taken from Ref. [42], while the energy spectra of the fission γ-rays were taken from the experimental work of [43], as described in detail in Ref. [18]. It is worth noting that the composition of dry air in the vicinity of the ^{252}Cf source was simulated by its main constituents O and N, which account for about 78% and 21% of the volume, respectively. However, hydrogen is present in dry air at an estimated concentration of 0.5 ppm per volume [44]. Since the ^{252}Cf fast neutrons may be moderated by the hydrogen in the water vapor, resulting in a lower neutron flux density towards the soil, this systematic error of the MCNP should be taken into account in operational areas with high levels of humidity (concentration of water vapor in air).

2.2. The (reflector/shield) assembly

2.2.1. The reflector

The cylindrical Be-reflector was introduced to reflect neutrons emitted in the direction away from the sample location, thus intensifying the neutron population that contributes to landmine detection. To determine the range over which the Be-thickness can be optimized as a reflector, the mean free path (λ) for Be at the most probable energy of the ^{252}Cf source (0.7 MeV) was calculated. This is done because at thicknesses greater than 1 λ, the 0.7 MeV neutrons may be moderated enough to be favored by reactions other than elastic scattering (e.g., (n,γ) reactions) in the increasing thickness of Be, reducing the neutron flux density towards the APM. The mean free path was calculated using the formula [45]:

$$\lambda = \frac{1}{\Sigma_T} \tag{2}$$

Where Σ_T (cm^{-1}) is the total macroscopic cross section determined by:

$$\sum_T = N\sigma_T \tag{3}$$

Where N is the atomic number density and σ_T is the total microscopic cross section.

With N calculated to be about 1.24×10^{23} atoms.cm^{-3} for Be and σ_T of about 3.449 b at 0.7 MeV [23], the value of the Σ_T was calculated to be about 0.428 cm^{-1}, resulting in a value for the mean free path of about 2.3 cm. Based on these considerations, the thickness of the Be-reflector was varied in steps of 1 cm over a range of 0–3 cm.

2.2.2. The shield

A considerable amount of neutrons may diffuse out of the Be-reflector, increasing the thermal background neutrons counted by the ^{3}He detectors. On the other hand, the diffused neutrons, in addition to the γ-rays accompanying the ^{252}Cf source, contribute to the total dose equivalent rate for the user. To address this issue, a cylindrical shielding layer was introduced and positioned concentrically on top of the Be-reflector. Considering the portability requirements due to size and weight, the performances of the $Zr(BH_4)_4$ and $Be(BH_4)_2$ shields were investigated by varying the thickness in 1 cm increments over a range of 0–3 cm.

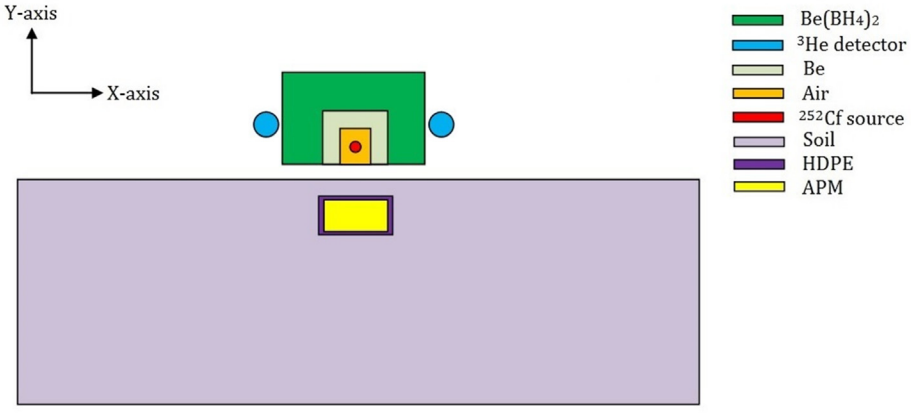

Fig. 1. Geometry as modeled in the MCNP simulations for the ^{252}Cf-NBT assembly.

2.3. Neutron detectors

The two ^{3}He detectors were simulated as identical cylinders filled with ^{3}He with the same dimensions used for the laboratory measurements reported in Ref. [14]. The two ^{3}He detectors were used to simulate only the number of thermal neutrons detected by the ^{3}He(n,p)^{3}H reaction. However, recent studies have confirmed that the physical ^{3}He detectors respond to fast neutrons with a sensitivity on the order of 10^{-3} [46,47]. To avoid such a systematic error and improve the accuracy of the MCNP results, both ^{3}He detectors were placed 3 cm above the ^{252}Cf source to reduce the background due to fast neutrons potentially counted by the physical ^{3}He detectors.

2.4. The plastic APM

The plastic anti-personnel mine APM used in this study was simulated by TNT with a density of 1.7 g/cm^{3} in the form of a cylindrical disc with a diameter of 7 cm and a height of 4 cm enclosed in a cylindrical disc of high-density polyethylene (HDPE) with a density of 0.955 g cm^{-3}, a diameter of 8 cm, and a height of 5 cm. The plastic APM was buried in a soil bed with the same dimensions as the laboratory measurements in Ref. [14] and a density of 1.5 g cm^{-3}.

It is worth noting that the hydrogen content in the plastic HDPE (C_2H_4) casing was estimated to be about 67 atoms%. This high content enriches the total amount of hydrogen in the APM explosive and increases the sensitivity of the proposed NBT model. On the other hand, APM was selected due to its small size and low hydrogen content, which is a challenging scenario against which to investigate the detection capabilities of the proposed NBT sensor. The assumed compositions of soil type, TNT explosive, HDPE, $Zr(BH_4)_4$, $Be(BH_4)_2$, and air as modeled in the MCNP simulations are listed in Table 1.

3. Calculation procedure and results

3.1. ^{3}He–^{3}He distance

The distance between the two ^{3}He detectors with the ^{252}Cf source (without reflector) in the center and 3 cm below was optimized by counting the S/B ratio, while the (^{3}He–^{3}He) distance was varied in steps of 2 cm in a range of 4–16 cm along the X-axis, away from the ^{252}Cf source. This is done at stand-off distance of 5 cm with the APM buried 3 cm deep in dry soil. The signals (I) (with landmine) and (I_o) (without landmine) counted by the two ^{3}He detectors were averaged and the S/B ratio was then calculated for each particular ^{3}He–^{3}He distance. It is worth noting that the current calculation procedure for the S/B ratio is applied to determine the effects of the other parameters.

The results are reported in Fig. 2. As can be seen, Fig. 2 shows that the S/B ratio increases with increasing ^{3}He–^{3}He distance in the range of 4–8 cm, reaching the highest value 0.512 reached at 8 cm. On the other hand, in the range of 8–16 cm, the S/B ratio decreases with increasing ^{3}He–^{3}He distance, with the lowest value 0.220 observed at 16 cm. This trend can be attributed to the solid angle (Ω) through which the backscattered neutron flux is transported in the direction of the two ^{3}He detectors. The results indicate that the backscattered neutron flux penetrates a virtual circular disc with a diameter (R) equal to that of the APM under study (8 cm) and a surface area of $\pi(R/2)^2$.

Thus, as long as ^{3}He–^{3}He $\leq$ 8 cm, the signals (I) are high enough to maintain an ascending order of the S/B ratio, reaching the highest value at ^{3}He–^{3}He = 8 cm. The highest S/B ratio may be attributed to the lowest background (I_o) at this point. However, as long as ^{3}He–^{3}He > 8 cm, the signals (I) are low enough to maintain a descending order of S/B ratio, with the lowest value observed at the largest ^{3}He–^{3}He distance studied of 16 cm. It is worth noting that 16 cm was selected as the ^{3}He–^{3}He distance corresponding to the worst case (lowest (S/B) ratio) against which the efficiency of the proposed reflector/shield configuration is to be examined.

3.2. Reflector thickness

The optimal thickness of the Be-reflector was determined by counting the S/B ratio, while the thickness was varied in 1 cm increments over a range of 0–3 cm. This was done with a ^{3}He–^{3}He distance of 16 cm, stand-off distance of 5 cm, and an APM burial

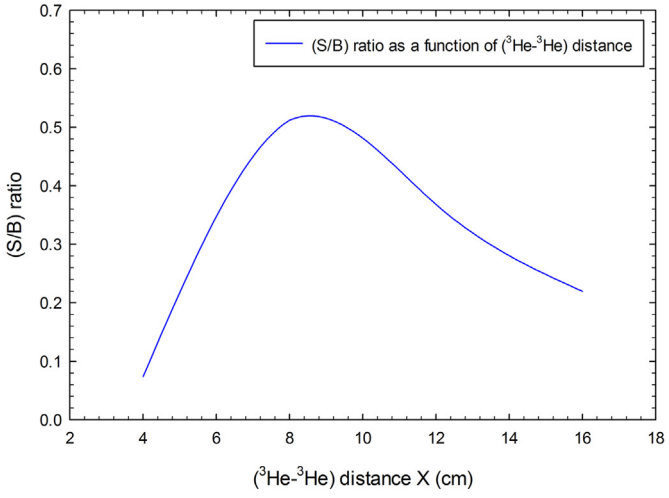

Fig. 2. Signal to background ratio S/B as a function of ^{3}He–^{3}He distance.

Table 1
Compositions of soil type, TNT explosive, HDPE, $Zr(BH_4)_4$, $Be(BH_4)_2$, and air as modeled in the MCNP simulations (rounded off).

Material	ρ (g.cm^{-3})	Mass fractions														
		H	Be	C	N	O	^{10}B	^{11}B	Na	Mg	AL	Si	K	Ca	Fe	Zr
Dry soil	1.5	0.010				0.515			0.006	0.013	0.070	0.266	0.016	0.050	0.054	
H (4 wt%)	1.5	0.040				0.537			0.003	0.012	0.066	0.240	0.015	0.045	0.042	
H (6 wt%)	1.5	0.060				0.530			0.005	0.016	0.055	0.245	0.014	0.033	0.042	
H (10 wt%)	1.5	0.100				0.541			0.004	0.011	0.043	0.228	0.013	0.034	0.026	
H (14 wt%)	1.5	0.140				0.501			0.004	0.011	0.043	0.228	0.013	0.034	0.026	
TNT	1.7	0.238		0.333	0.143	0.286										
HDPE	0.95	0.143		0.857												
$Zr(BH_4)_4$	1.18	0.107					0.057	0.230								0.060
$Be(BH_4)_2$	0.604	0.208		0.233			0.111	0.448								
Air	0.0012				0.756	0.244										

depth of 3 cm in dry soil. The results are shown in Fig. 3. As can be observed in Fig. 3, the S/B ratio increases as reflector thickness increases, reaching the highest value of about 786 at 2 cm.

The resulting optimal thickness of 2 cm is reasonable, as it is comparable to the 1 λ thickness of 2.3 cm calculated for Be at the most probable energy of the ^{252}Cf source neutrons of 0.7 MeV. The difference may be attributed to the different nature of the two calculation methods: The analytical approach uses a mathematical equation to determine λ, while the MCNP simulations estimate the value of λ by modeling the problem using the cross section data libraries associated with the MCNP code. In addition, the difference may also be attributed to the uncertainties in the material composition as well as the statistical errors in the MCNP results, which were reported to be about 0.03%. In addition, Fig. 3 shows that the S/B ratio decreases with increasing reflector thickness for thicknesses greater than 2 cm, with the lowest value observed at 3 cm.

This can be attributed to the decrease in the signal (I) due to the decrease in the number of neutrons elastically scattered by Be towards the APM location, and the increase in the background (I_o) due to the moderated neutrons possibly diffusing from the reflector towards the ^{3}He detectors. At this point, 2 cm was selected as the optimal reflector thickness and the NBT geometry was considered to be a^{252}Cf source encapsulated in a cylindrical Be-reflector of 2 cm thickness and positioned at the midpoint between and 3 cm below two ^{3}He detectors located ±8 cm along the X-axis from the ^{252}Cf source.

3.3. Shield thickness

The optimal shield thickness was determined by calculating the total dose equivalent rate (D_{Total}), while the shield thickness was increased in steps of 1 cm in the range of 0–3 cm. It is worth noting that in the current MCNP dose calculations, the ambient dose equivalent was selected to estimate the efficiency of the proposed shield. It was calculated by considering the operational quantity H*(10) as a reasonable assessment of the effective dose for our current portable NBT model [48].

The shield thickness was increased, while the thickness of the Be-reflector was fixed at 2 cm. For each shield thickness, the D_{Total} value at 100 cm above the shield was calculated using the flux tally at a point (F5). The normalized neutron and gamma radiation fluxes were converted to dose equivalent rates using the MCNP5 dose energy (DE) and the dose function (DF), and the results are given in (mSv/h). The total dose equivalent rate was calculated as $D_{Total} = D(n)+D(\gamma)$, where D(n) and D(γ) are the total dose equivalent rates for neutrons and gamma, respectively. D(γ) is calculated as $D(\gamma) = D\gamma_{(source)}+D\gamma_{(n,\gamma)}$, where $D\gamma_{(source)}$ and $D\gamma_{(n,\gamma)}$ are the dose equivalent rates due to primary γ-rays from the ^{252}Cf source and secondary γ-rays released by (n,γ) reactions in the shield, respectively.

3.3.1. Neutron dose equivalent rate (D(n))

The D(n) values due to neutrons potentially diffusing from the proposed shield were calculated as a function of shield thickness and shown in Fig. 4. As can be seen in Fig. 4, the overall D(n) values for both the $Be(BH_4)_2$ and $Zr(BH_4)_4$ shields decrease with increasing thickness across all thicknesses, with the lowest values (for both shields) obtained at 3 cm. The curve for each shield differs slightly by a factor with increasing density, with $Zr(BH_4)_4$ being the shield with the lowest D(n) values across all thicknesses. At 3 cm thickness, the D(n) value of $Zr(BH_4)_4$, 0.001481 mSv/h, is about 0.5% lower than that of $Be(BH_4)_2$, 0.001489 mSv/h.

To investigate such results, the effective fast neutron removal cross section Σ_R (cm^{-1}) for both shielding materials was calculated using the partial density of the elements and their mass removal cross sections as described in Ref. [18]. The results are presented in Table 2. As can be observed in Table 2, the total Σ_R value of 0.055 cm^{-1} for $Zr(BH_4)_4$ exceeds the value of 0.053 cm^{-1} calculated for $Be(BH_4)_2$ by about 3.8%. Since the Σ_R values for hydrogen and boron are similar for both shields (Table 2), the higher Σ_R value calculated for $Zr(BH_4)_4$ can be attributed mainly to the presence of Zr with a partial effective fast neutron removal cross section $\Sigma_{R(Zr)}$ = 0.0112 cm^{-1}, which is about 17.9% higher than the $\Sigma_{R(Be)}$ = 0.0095 cm^{-1} calculated for Be. Thus, a larger number of neutrons in $Zr(BH_4)_4$ are sufficiently thermalized to be absorbed by the ^{10}B(n,α)^{7}Li reaction, which reduces the neutron dose equivalent rate D(n). This result explains the conclusion of Hayashi et al. (2009) [30]: atoms with high-Z content such as Zr are as effective as hydrogen atoms in neutron shielding. Therefore, the superiority of $Zr(BH_4)_4$ in reducing the neutron dose equivalent rate D(n) is reasonable.

3.3.2. Gamma dose equivalent rate ($D\gamma_{(n,\gamma)}$)

The $D\gamma_{(n,\gamma)}$ values due to secondary γ-rays released by (n,γ) reactions in the shields were calculated as a function of shielding thickness. The results for $Be(BH_4)_2$ and $Zr(BH_4)_4$ were compared and presented in Fig. 5. As can be seen in Fig. 5, the $D\gamma_{(n,\gamma)}$ values for

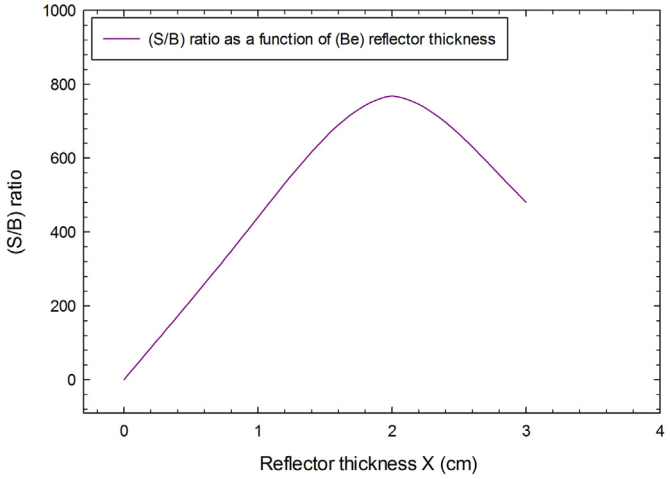

Fig. 3. Signal to background ratio S/B as a function of reflector thickness.

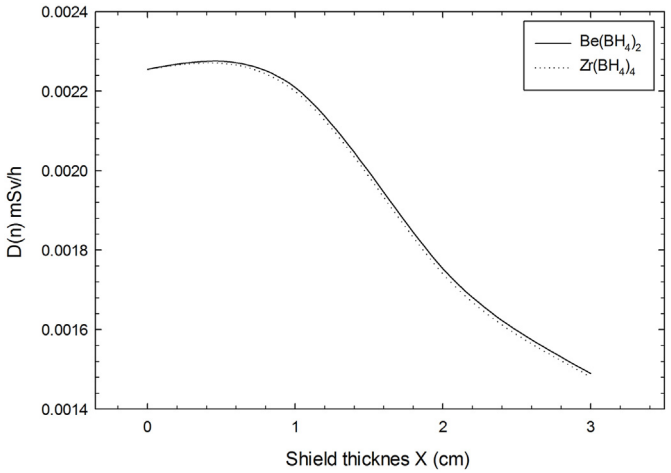

Fig. 4. The neutron dose equivalent rate D(n) as a function of shield thickness.

Table 2
Effective fast neutron removal cross section Σ_R (cm^{-1}) values for shielding materials.

Element	$Be(BH_4)_2$ (0.604 g cm^{-3})			$Zr(BH_4)_4$ (1.18 g cm^{-3})		
	Partial density	Σ_R/ρ ($cm^2.g^{-1}$)	Σ_R (cm^{-1})	Partial density	Σ_R/ρ ($cm^2.g^{-1}$)	Σ_R (cm^{-1})
H	0.1256	0.1900	0.0239	0.1263	0.1900	0.0240
^{10}B	0.0670	0.0575	0.0039	0.0673	0.0575	0.0039
^{11}B	0.2706	0.0575	0.0156	0.2714	0.0575	0.0156
Be	0.1407	0.0678	0.0095			
Zr				0.7151	0.0156	0.0112
Total (Rounded off)	0.604	0.373	0.053	1.18	0.321	0.055

both shields decrease gradually over the thickness range of 0–2 cm, while a rapid decrease was observed as the thickness increased in the range of 2–3 cm.

This trend could be attributed to the rates of (n,γ) reactions in the shield, which differ with the thickness of the shield. The fast neutrons that are moderated in the Be reflector and diffuse into the shield are further moderated enough to be captured by hydrogen via $^1H(n,\gamma)^1H$ or absorbed by ^{10}B via $^{10}B(n,\gamma)^7Li$ reactions. Consequently, the gradual decrease in the range of 0–2 cm thickness can be mainly attributed to the γ-emission rate by $^1H(n,\gamma)^1H$, which could be high enough compared to the thermal neutron absorption rate by the $^{10}B(n,\gamma)^7Li$ reaction for both shields to maintain this trend. The rapid decrease in the 2–3 cm thickness range may be attributed to the increase in boron density with increasing thickness of both shields, which leads to significantly higher thermal neutron absorption rates of by $^{10}B(n,\gamma)^7Li$, decreasing the number of thermal neutrons captured by $^1H(n,\gamma)^1H$. Consequently, the dose equivalent rate $D\gamma_{(n,\gamma)}$ due to (n,γ) reactions is reduced.

Likewise in Fig. 4, the graph of each shield decreases by a factor as shield density increases, with $Zr(BH_4)_4$ being the shield with the lowest $D\gamma_{(n,\gamma)}$ values across all thicknesses. In addition to the higher density of 1.18 g cm^{-3}, the preference for $Zr(BH_4)_4$ is promoted by the photoelectric absorption process, which favors high Z number absorbers such as Zr (Z = 40), present in $Zr(BH_4)_4$ with an atomic number density of 0.5 × 1022 atoms.cm^{-3}. At a thickness of 3 cm, the results show that the $D\gamma_{(n,\gamma)}$ value of 0.0002 mSv/h achieved by $Zr(BH_4)_4$ is 50% lower than the value of 0.0004 mSv/h calculated for $Be(BH_4)_2$.

3.3.3. Gamma dose equivalent rate ($D\gamma_{(source)}$)

The $D\gamma_{(source)}$ values due to the primary γ-ray flux associated with the ^{252}Cf source were calculated as a function of shielding thickness, and the results are reported in Fig. 6. As can be observed in Fig. 6, the $D\gamma_{(source)}$ values across all thicknesses decrease with increasing thickness for both $Be(BH_4)_2$ and $Zr(BH_4)_4$ shields, with the lowest values obtained at 3 cm. The curve of each shield differs by a factor as density increases, with $Zr(BH_4)_4$ being the shield with the lowest $D\gamma_{(source)}$ values across all thicknesses. This is due to the optimal gamma shielding potential of $Zr(BH_4)_4$, which is achieved by the presence of a high-Z element (Zr). At a thickness of 3 cm, $Zr(BH_4)_4$ achieves a $D\gamma_{(source)}$ value of about 0.001 mSv/h, which is about 16.7% lower than the value of about 0.0012 mSv/h achieved by $Be(BH_4)_2$.

3.3.4. Total dose equivalent rate (D_{Total})

The D_{Total} values were calculated for each shield thickness and the results are shown in Fig. 7. As can be seen in Fig. 7, the D_{Total} values for both $Be(BH_4)_2$ and $Zr(BH_4)_4$ shields decrease as thickness increases, with the lowest values (for both shields) obtained at 3 cm. The curve for each shield differs by a factor as density increases, with $Zr(BH_4)_4$ being the shield with the lowest D_{Total} values across all thicknesses.

At a thickness of 3 cm, the D_{Total} value of 0.0027mSv/h achieved by $Zr(BH_4)_4$ is about 12.9% lower than the value of 0.0031 mSv/h determined for $Be(BH_4)_2$. Compared with the D_{Total} value of 0.0049 mSv/h calculated without shielding, i.e., with a 2 cm thick Be-reflector, both $Zr(BH_4)_4$ and $Be(BH_4)_2$ shields reduce the D_{Total} value by about 44.9% and 36.7%, respectively. On the other hand, the S/B ratio of 925 calculated for $Zr(BH_4)_4$ at a shielding thickness of 3 cm is about 4.4% higher than the value of 886 calculated for $Be(BH_4)_2$. However, compared with the S/B ratio of 768 calculated at the optimal thickness (2 cm) for the Be-reflector, both $Zr(BH_4)_4$ and $Be(BH_4)_2$ shields effectively increased the S/B ratio by about 20% and 15%, respectively.

At this point, 3 cm was selected as the optimal shielding

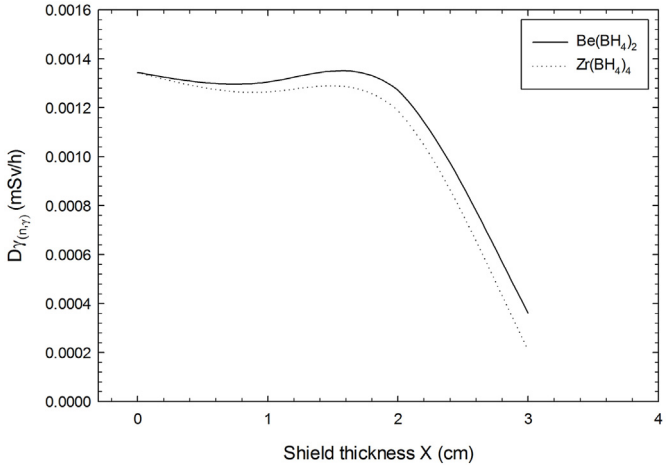

Fig. 5. The gamma dose equivalent rate $D\gamma_{(n,\gamma)}$ as a function of shield thickness.

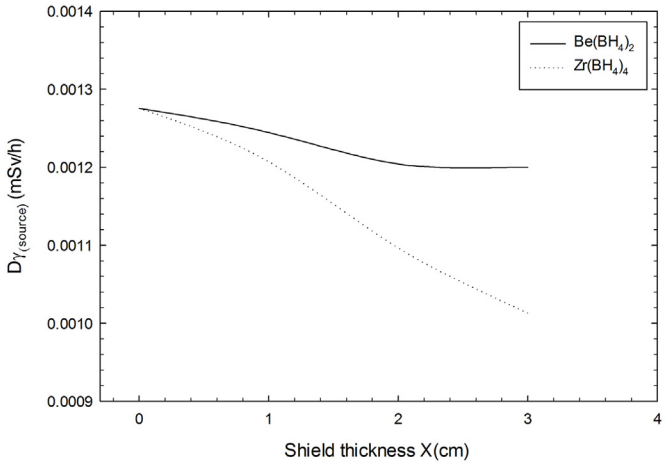

Fig. 6. The gamma dose equivalent rate $D\gamma_{(source)}$ as a function of shield thickness.

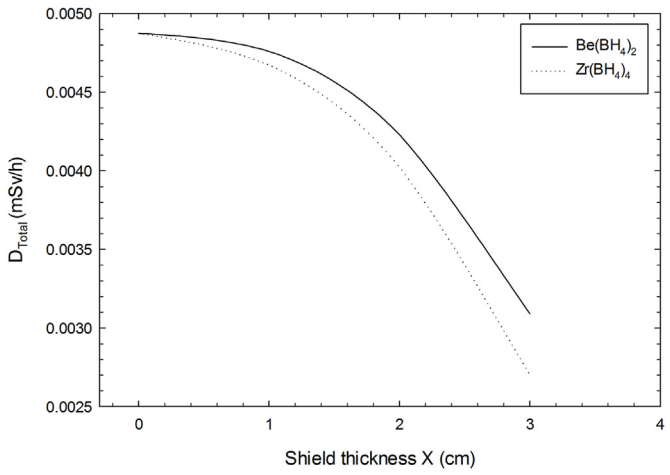

Fig. 7. The total dose equivalent rate D_{Total} as a function of shield thickness.

thickness, and 2 cm Be/3 cm $Zr(BH_4)_4$ as well as 2 cm Be/3 cm $Be(BH_4)_2$ were determined to be the optimal reflector/shied configurations for the currently proposed ^{252}Cf-based NBT model sensor. The overall size for each optimal configuration was calculated to be 13 cm diameter × 10 cm height. The results in terms of D_{Total} indicate that our proposed ^{252}Cf-based NBT sensor with the 2 cm Be/3 cm $Zr(BH_4)_4$ or 2 cm Be/3 cm $Be(BH_4)_2$ configurations can operate for about 925 and 806 days, respectively, at a work load of 8 h/day, within the requirements of the annual allowable dose limit for radiological workers of 20 mSv [13].

It is worth noting that the S/B value obtained with the 2 cm Be/3 cm $Zr(BH_4)_4$ cylindrical configuration was higher by factors of about 28.9 and 1.32, respectively, than the values reported in Ref. [14] from the laboratory-optimized NBT device (32) or the values calculated by the NBT model with the cube-shaped C/$Zr(BH_4)_4$ assembly (700). With the 2 cm Be/3 cm $Be(BH_4)_2$ configuration, an increase by factors of about 27.7 and 1.27, respectively, was achieved. On the other hand, the permissible operating days due to the D_{Total} for the current optimal NBT model with the 2 cm Be/3 cm $Zr(BH_4)_4$ or 2 cm Be/3 cm $Be(BH_4)_2$ configurations exceed the 250 days permitted by the D(n) value of 0.01 mSv/h for the NBT model with C/$Zr(BH_4)_4$ assembly [14] by factors of about 3.7 and 3.5, respectively.

Based on these considerations, as well as the moderately low toxicity and lower price of Zr compared to Be [49–51], the results clearly suggest 2 cm Be/3 cm $Zr(BH_4)_2$ as the optimal and cost-effective configuration. However, the weight of the 2 cm Be/3 cm $Be(BH_4)_2$ configuration, about 1.07 Kg, was found to be about 36% less than that of the 2 cm Be/3 cm $Zr(BH_4)_2$ configuration, about 1.68 Kg. Moreover, the abundance of ^{9}Be (100%) exceeds that of ^{40}Zr (51.45%) [52] by a factor of about 1.9. Therefore, in terms of portability and abundance of Be, the 2 cm Be/3 cm $Be(BH_4)_2$ configuration was preferred and selected for the rest of calculations.

3.4. Stand-off distance

The stand-off distance was varied in 2.5 cm increments over the range 2.5–15 cm, while the APM burial depth was fixed at 3 cm. S/B ratios were calculated considering a dry soil with a hydrogen content of 1 wt%, and the results are presented in Fig. 8. As can be seen in Fig. 8, the highest S/B ratio was reached at stand-off distance of 2.5 cm. For stand-off distances in the range of 5–15 cm, the S/B ratio decreases with increasing stand-off distance, with the lowest S/B value observed at stand-off distance of 15 cm.

The results reported in Fig. 8 suggest 2.5 cm as the optimal stand-off distance. However, to reduce the risk of triggering APM explosion, stand-off distance of 5 cm was selected and the corresponding S/B ratio was calculated as 886.

3.5. Burial depth

The APM burial depth was increased in increments of 1 cm in the range of 0–5 cm, while the stand-off distance was fixed at 5 cm. The range of APM burial depth was considered because Anti-personnel mines are usually shallow buried at a range from flush with the surface to a maximum depth of about 5 cm, as they cause less damage if buried any deeper [31]. The S/B ratios were calculated considering a dry soil with a hydrogen content of 1 wt% and the results were reported in Fig. 9. As can be seen in Fig. 9, the highest S/B ratio across all burial depths was obtained when the APM was flush with the soil surface (burial depth = 0 cm). For burial depths of 1–5 cm, the S/B ratio decreases as the burial depth increases, with the lowest S/B value observed at a burial depth of 5 cm. The results reported in Fig. 9 indicate that (0 cm) is the optimal burial depth. However, in this work, a shallow burial depth of 3 cm was considered and the corresponding S/B ratio was calculated, showing a similar value as in Fig. 8.

3.6. Soil density

The sensitivity of the selected model to soil density was investigated at stand-off distance of 5 cm and APM burial depth of 3 cm. For this purpose, the density of the dry soil was varied at a constant hydrogen content of 1 wt% in increments of 0.3 g cm^{-3} and over the range of 1.2–2.1 g cm^{-3}. The results are reported in Fig. 10. As can be observed in Fig. 10, the S/B ratio decreases as soil density increases across all soil densities, with the lowest value 247 observed at 2.1 g cm^{-3}.

This trend can be attributed to the fact that an increase in bulk density increases the density of the neutron-affecting minerals in the soil [53]. The scattering properties and the content of these minerals per unit volume of soil determine the macroscopic scattering cross section of soils. Thus, when the bulk density increases, the macroscopic scattering cross section increases [54]. These facts could explain the current MCNP results as well as the laboratory measurements performed by Marais &Smit (1962) [55], which showed that the count rate (due to backscattered thermal

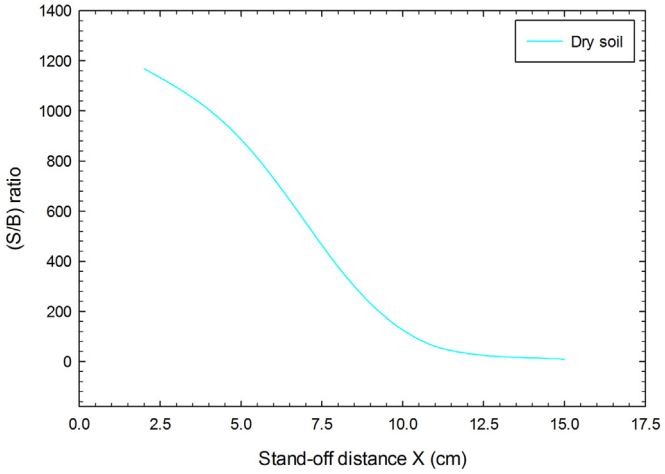

Fig. 8. Signal to background ratio S/B as a function of stand-off distance.

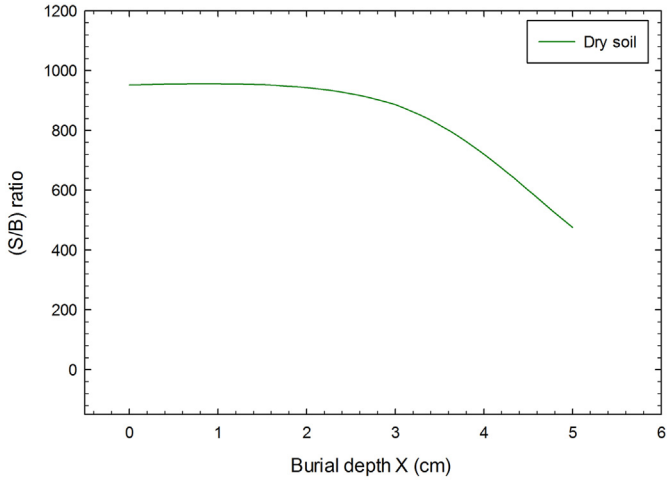

Fig. 9. Signal to background ratio S/B as a function of APM burial depth.

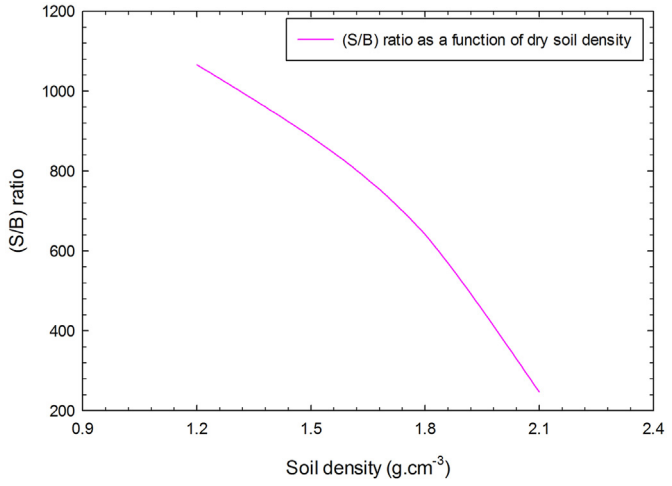

Fig. 10. Signal to background ratio S/B as a function of dry soil density.

neutrons) for a neutron moisture meter increased considerably as the bulk density of the soil increased, although the percent moisture content remained constant. Thus, it can be concluded that the background (I_o) due to the backscattered flux of slow neutrons is proportional to the bulk density of the soil containing the mine.

3.7. APM scanning

The NBT model ^{252}Cf-2 cm Be/3 cm Be$(BH_4)_2$ was scanned at stand-off distance of 5 cm across the center of the APM when buried 3 cm deep in dry soil containing 1 wt% hydrogen and moist soil containing 4–14 wt% hydrogen. The soil density was kept constant at 1.5 g cm^{-3} for all soil types. This is done to eliminate the influence of soil density and to allow an accurate evaluation of the effects of soil hydrogen content. Scans were taken over a distance of 50 cm along the X-axis with a step size of 5 cm and an acquisition time of 100 s. The results are presented in Fig. 11 as variations of the S/B ratio as a function of the position of the ^{252}Cf source.

As can be seen in Fig. 11, across all source positions, the maximum (S/B) ratios are observed whenever the ^{252}Cf-2 cm Be/3 cm Be$(BH_4)_2$ assembly crosses the center of the APM, i.e., at X = 0 cm. Furthermore, the curve of each soil type differs by a factor as the hydrogen content increases, with the lowest S/B ratios

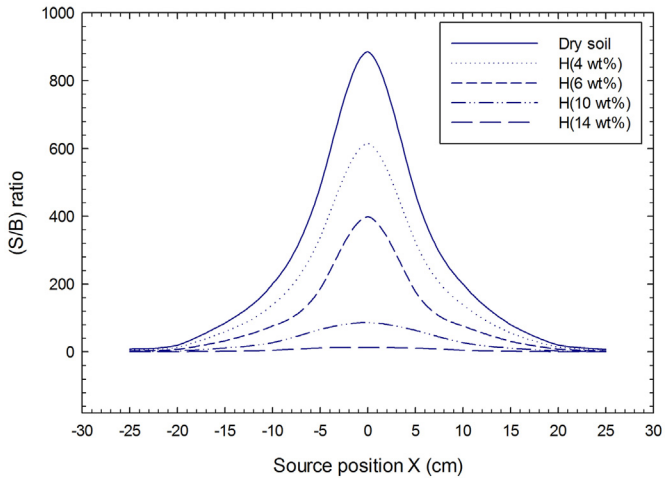

Fig. 11. Scans with shielded ^{252}Cf-2 cm Be/3 cm Be$(BH_4)_2$ NBT model across the center of plastic APM buried in dry soil with 1 wt% hydrogen and moist soils with (4–14) wt% hydrogen.

observed at 14 wt% across all source positions. At the source position (X = 0 cm), S/B values were determined in descending order: 886, 615, 398, 86, and 12 for dry soils with 1 wt% hydrogen and moist soils with 4, 6, 10, and 14 wt% hydrogen, respectively. At this point, it can be concluded that our proposed model ^{252}Cf-2 cm Be/3 cm Be$(BH_4)_2$ at stand-off distance of 5 cm and APM burial depth of 3 cm is suitable for APM detection in both dry and moist soils with 1–14 wt% hydrogen and achieves S/B ratios in the range of 886-12, with the optimal working conditions observed for dry soils with 1 wt% hydrogen.

4. Future outlook

The currently proposed reflector/shield model has effectively reduced the D_{Total} to 0.0031mSV/h, allowing 208 days of operation for a work load of 8 h/day. To reduce the D_{Total} and increase the allowable duration of the current NBT model, further optimization of shielding should be considered. However, the radiation protection requirements of a human user may necessitate the use of heavy shielding at the expense of the portability desired for a hand-held NBT sensor. In addition, the hazardous deployment area of such devices carries the risk of a possible mine explosion that could be triggered by the proposed probe. For these reasons, the possible use of such devices as unmanned robotic sensors is suggested for future work.

On the other hand, the use of ^{3}He detectors in the current NBT model was motivated by their high efficiency in detecting thermal neutrons, which is achieved by the significantly high absorption cross section for the ^{3}He(n,p)^{3}H reaction. Due to the increasing cost of ^{3}He detectors [40] caused by the increasing shortage of ^{3}He, future work should consider the possible use of alternative non-^{3}He detectors with lower cost and reasonable efficiency. In this regard, there are several potential ^{3}He replacement technologies such as: Ar/CO_2-gas filled detectors coated with B_4C [56], ^{10}B/ZnS(Ag) [41] and Cs_2LiYCl_6(CLYC) [57] scintillation detectors, have been identified as interesting alternatives for ^{3}He detectors.

5. Conclusion

Comparative MCNP optimizations were performed to investigate the applicability of the cylindrical assemblies Be/Be$(BH_4)_2$ and Be/Zr$(BH_4)_4$ as possible replacements for the cube-shaped

assembly C/Zr$(BH_4)_4$ reported in Ref. [14]. Each reflector/shield was configured to encapsulate a 100 MBq ^{252}Cf source centered between two identical ^{3}He detectors. The performance of each configuration was evaluated in terms of increasing the S/B ratio for a buried APM and minimizing D_{Total} for the operator.

The results show that 2 cm Be/3 cm Zr$(BH_4)_4$ and 2 cm Be/3 cm Be$(BH_4)_2$ are the optimal shielding configurations with S/B ratios of 925 and 886, respectively, as APM is buried in dry soil. Compared with the S/B ratio of 768 obtained by Be-reflector at its optimal thickness (2 cm) without shielding, it can be concluded that the 2 cm Be/3 cm Zr$(BH_4)_4$ and 2 cm Be/3 cm Be$(BH_4)_2$ configurations effectively increase the S/B ratio by about 20% and 15%, respectively. On the other hand, the results show that 2 cm Be/3 cm Zr$(BH_4)_4$ and 2 cm Be/3 cm Be$(BH_4)_2$ produce D_{Total} values of about 0.0027 mSv/h and 0.0031 mSv/h, respectively. Compared with the D_{Total} value obtained with a 2 cm thick Be-reflector (0.0049 mSv/h), it is found that the 2 cm Be/3 cm Zr$(BH_4)_4$ and 2 cm Be/3 cm Be$(BH_4)_2$ configurations significantly reduce the D_{Total} value by about 44.9% and 36.7%, respectively.

On the other hand, as reported in Ref. [14], the S/B values measured with the laboratory-optimized NBT device (32) or calculated with the NBT model with the cube-shaped C/Zr$(BH_4)_4$ assembly (700) were increased in the current study by factors of about 28.9 and 1.32, respectively, with the 2 cm Be/3 cm Zr$(BH_4)_4$ configuration and by factors of about 27.7 and 1.27, respectively, with the 2 cm Be/3 cm Be$(BH_4)_2$ configuration. Moreover, the allowable operating days due to D_{Total} for the 2 cm Be/3 cm Zr$(BH_4)_4$ and 2 cm Be/3 cm Be$(BH_4)_2$ configurations exceed those allowed (due to D(n)) for the NBT model with C/Zr$(BH_4)_4$ assembly by factors of about 3.7 and 3.5, respectively.

These facts confirm the applicability of the two current cylindrical reflector/shield configurations as potential replacements for the cube-shaped C/Zr$(BH_4)_4$ assembly, with 2 cm Be/3 cm Zr$(BH_4)_4$ being the optimal configuration. However, it was found that the weight of the 2 cm Be/3 cm Be$(BH_4)_2$ configuration is about 36% lower than that of the 2 cm Be/3 cm Zr$(BH_4)_4$ configuration. In addition, the abundance of ^{9}Be is higher than that of ^{40}Zr by a factor of 51.45%. Therefore, the 2 cm Be/3 cm Be$(BH_4)_2$ configuration was selected with respect to the portability and abundance of ^{9}Be.

The sensitivity of the selected ^{252}Cf-2cm Be/3 cm Be$(BH_4)_2$ NBT model to soil density was investigated at stand-off distance of 5 cm and APM buried 3 cm deep in dry soil with a constant hydrogen content of 1 wt%. The result shows that the S/B ratio decreases as soil density increases, with descending values: 1066, 886, 641, and 247 for soil with densities of 1.2 g cm^{-3}, 1.5 g cm^{-3}, 1.8 g cm^{-3}, and 2.1 g cm^{-3}, respectively. However, given the considerable S/B ratios obtained, it can be concluded that the selected model is suitable for the identification of APMs in soils with densities in the range of 1.2–2.1 g cm^{-3}.

The effect of soil hydrogen content on the performance of the selected ^{252}Cf-2 cm Be/3 cm Be$(BH_4)_2$ NBT model was determined at different source positions while scanning at stand-off distance of 5 cm above the center of the APM when it was buried 3 cm deep in dry and moist soils. The results confirmed that our proposed ^{252}Cf-2 cm Be/3 cm Be$(BH_4)_2$ NBT model positively identified the plastic APM over all hydrogen concentrations investigated (1–14) wt% and at 100 s acquisition time. At the point (X = 0 cm) where the ^{252}Cf source crosses the center of the APM, the S/B ratios were calculated and shown to have the descending order: 886, 615, 398, 86, and 12 for dry soils with 1 wt% hydrogen and for moist soils with 4, 6, 10, and 14 wt% hydrogen, respectively.

Given the size of the ^{252}Cf-2 cm Be/3 cm Be$(BH_4)_2$ NBT model with 13 cm diameter × 10 cm height, a weight of 1.07 Kg, and a total dose equivalent rate of 0.0031 mSV/h, the MCNP results suggest the applicability of the proposed NBT sensor as a hand-held portable device. With a work load of 8 h/day, the proposed NBT device can be operated within the 20 mSV annual permissible dose limit for 806 days.

Declaration of competing interest

The authors declare that they have no known competing financial interests or personal relationships that could have appeared to influence the work reported in this paper.

Acknowledgement

The author thanks the Dipartimento di Fisica degli Universita di Padova and INFN sezione di Padova, for hosting the experimental activities in collaboration with the ICTP-IAEA Sandwich Training Educational Program (STEP). Special thanks are due to Dr. Ibrahim ElAgib from King Saud University for valuable discussions on the properties of MCNP.

References

[1] H. Killers, The Global Land-Mine Crisis, Report Released by the US Department of State, Bureau of Political-Military Affairs, Office of Humanitarian De-mining Programs, Washington, DC, 1998.
[2] G. Vourvopoulos, P.C. Womble, Pulsed fast/thermal neutron analysis: a technique for explosives detection, Talanta 54 (2001) 459–468.
[3] N. Elsheikh, G. Viesti, I. ElAgib, F. Habbani, On the use of a (^{252}Cf-^{3}He) assembly for landmine detection by the neutron back-scattering method, Appl. Radiat. Isot. 70 (2012) 643–649.
[4] S.F. Masoudi, M. Ghashami, D-T neutron generators as a feasibility tool for landmine detection based on neutron backscattering method, Ann. Nucl. Energy 65 (2014) 441–445.
[5] G. Vourvopoulos, R.A. Sullivan, Evaluation of PELAN as a landmine confirmation sensor, Proc. SPIE 6217 (2006) 1–6, 62171P.
[6] N.A.A. Elsheikh, Monte Carlo modelling of a neutron-induced gamma-ray sensor for landmine or explosive detection, J. Radiat. Res. Appl. Sci. 11 (2018) 403–407.
[7] S.A.I. Corporation, an Advanced ESTCP PELAN System for Surface and Near-Surface UXO Discrimination, ESTCP Project Number MM-200503, 2009.
[8] A.A.E. Nassreldeen, Characterization of (^{252}Cf-ZrH_2) Monte Carlo model for detection of nitrogen and chlorine by thermal neutron-capture PGNAA, Radiat. Phys. Chem. 188 (2021) 109591.
[9] E.M.A. Hussein, E.J. Waller, Landmine detection: the problem and the challenge, Appl. Radiat. Isot. 53 (2000) 557–563.
[10] V.R. Bom, C.P. Datema, C.W.E. Van Ejik, The status of the delft university neutron backscatter landmine detector (DUNBLAD), Appl. Radiat. Isot. 61 (2004) 21–25.
[11] F.D. Brooks, M. Drosg, The HYDAD-D anti-personnel landmine detector, Appl. Radiat. Isot. 63 (2005) 565–574.
[12] C.P. Datema, V.R. Bom, C.W.E. Van Eijk, Landmine detection with the neutron backscattering method, IEEE Nucl. Sci. Conf. Rec. 1 (2001) 5111–5114.
[13] C.P. Datema, V.R. Bom, C.W.E. Van Eijk, Experimental results and Monte Carlo simulations of a landmine localization device using the neutron backscattering method, Nucl. Instrum. Methods 488 (2002) 441–450.
[14] A.A.E. Nassreldeen, Multi-parameter optimization of a (^{3}He-^{252}Cf-^{3}He) neutron backscattering sensor for landmine detection, J. Radiat. Res. Appl. Sci. 10 (2017) 122–127.
[15] B. Kiraly, L. Olah, J. Csikai, Neutron-based techniques for detection of explosives and drugs, Radiat. Phys. Chem. 61 (2001) 781–784.
[16] J. Csikai, R. Doczi, B. Kiraly, Investigations on landmine detection by neutron-based techniques, Appl. Radiat. Isot. 61 (2004) 11–20.
[17] F.D. Brooks, M. Drosg, A. Buffler, M.S. Allie, Detection of anti-personnel landmines by neutron scattering and attenuation, Appl. Radiat. Isot. 61 (2004) 27–34.
[18] A.A.E. Nassreldeen, Gamma-ray and neutron shielding features for some fast neutron moderators of interest in ^{252}Cf-based boron neutron capture therapy, Appl. Radiat. Isot. 156 (2020) 109012.
[19] F.D. Brooks, M. Drosg, The HYDAD-D antipersonnel landmine detector, Appl. Radiat. Isot. 63 (2005) 565–574.
[20] Obhadas, D. Sudac, K. Nad, V. Valkovic, G. Nebbia, G. Viesti, The soil moisture and its relevance to landmine detection by neutron backscattering technique, Nucl. Instrum. Methods B 213 (2004) 445–451.
[21] M. Asnal, T. Liamsuwan, T. Onjun, An evaluation on the design of beam shaping assembly based on the D-T reaction for BNCT, J. Phys. Conf. 611 (2015), 012031.
[22] I. Elagib, A.M. Artoli, F. Habbani, M. Badawi, Monte Carlo simulation of Pu-Be, Am-Be and Cf-252 neutrons backscattering from buried explosives in dry soil, in: International Conference on Computer Applications Technology (ICCAT),

2013, pp. 1–4.
[23] National nuclear data center, Brookhaven National laboratory. https://www.nndc.bnl.gov/, 2008.
[24] R. Khabaz, Assessment of gamma-rays generated by the spontaneous fission source ^{252}Cf using a Monte Carlo method, Ann. Nucl. Energy 46 (2012) 76–80.
[25] A.A.E. Nassreldeen, Shielding capabilities of Mg $(BH_4)_2$, TiH_2, C_2H_4-25%B and C_2H_4 as ^{252}Cf neutron source shielding containers: Monte Carlo simulations, Afr. Rev. Phys. 15 (2020), 0013.
[26] T. Dhliwayo, Development of advanced shield systems for fast neutrons, Int. Nucl. Saf. J. 3 (2014) 49–53.
[27] F.A. Smith, A Primer in Applied Radiation Physics, Singapore: World Scientific Publishing Co.Pte.Ltd, Po Box 128, Farrer Road, Singapore, 2000, p. 912805.
[28] V.P. Singh, N.M. Badiger, Gamma ray and neutron shielding properties of some alloy materials, Ann. Nucl. Energy 64 (2014) 301–310.
[29] M.I. Sayyed, O. Agar, F. Akman, H.O. Tekin, M.R. Kaçal, An extensive investigation on gamma ray shielding features of Pd/Ag based alloys, Nucl. Eng. Technol. 51 (2019) 853–859.
[30] T. Hayashi, K. Tobita, Y. Nakamori, S. Orimo, Advanced neutron shielding material using zirconium borohydride and zirconium hydride, J. Nucl. Mater. (2009) 386–388.
[31] X-5 Monte Carlo Team, MCNP- a General Monte Carlo N-Particle Transport Code: Overview and Theory, vol. 5, Los Alamos National Laboratory, 2003. Revised 6/30/04).
[32] V. Bom, M.A. Ali, C.W.E. van Eijk, Land mine detection with neutron back scattering imaging using a neutron generator, EEE Trans. Nucl. Sci. 53 (2006) 356–360.
[33] B.C. Anderson, K.E. Holbert, H. Bowler, Design, Construction, and Modeling of a ^{252}Cf Neutron Irradiator, Science and Technology of Nuclear Installations, 2016, p. 9012747.
[34] J. Scherzinger, J.R.M. Annand, G. Davatz, K.G. Fissum, U. Gendottid, R. Hall-Wilton, A. Rosborg, E. H akansson, R. Jebali, K. Kanakib, M. Lundin, B. Nilsson, H. Svensson, Tagging fast neutrons from an ^{241}Am/^{9}Be source, Appl. Radiat. Isot. 98 (2015) 74–79.
[35] J.G. Fantidis, Comparison of different geometric configurations and materials for neutron radiography purposes based on a ^{241}Am/Be neutron source, J. Taibah Univ. Sci. 6 (2017) 1214–1220.
[36] Z.D. Whetstone, K.J. Kearfott, A review of conventional explosives detection using active neutron interrogation, J. Radioanal. Nucl. Chem. 301 (2014) 629–639.
[37] T.P. Lou, Compact D-D/d-T Neutron Generators and Their Applications, A Dissertation Submitted in Partial Satisfaction of the Requirements for the Degree of Doctor of Philosophy, University Of California, Berkeley, 2003.
[38] T.W. Crane, M.P. Baker, Neutron detectors. Chap. 13, passive nondestructive assay of nuclear materials, in: D. Reilly, et al. (Eds.), Technical Report NUREG/CR-5550; LA-UR-90-732, Los Alamos National Laboratory, NM, USA, 1991.
[39] D.R. Ochbelagh, Comparison of ^{3}He and BF_3neutron detectors used to detect hydrogenous material buried in soil, Radiat. Phys. Chem. 81 (2012) 379–382.
[40] K. Zeitelhack, Search for alternative techniques to helium-3 based detectors for neutron scattering applications, Sci. Rev. 23 (2012) 10–13.
[41] K.A. Guzman-Garcia, H.R. Vega-Carrillo, E. Gallego, J.A. Gonzalez-Gonzalez, A. Lorente, S. Ibañez-Fernandez, ^{10}B+ZnS(Ag) as an alternative to ^{3}He-based detectors for radiation portal monitors, EPJ Web Conf. 253 (2017), 07008.
[42] R.V. Griffith, J. Palfalvi, U. Madhvanath, Compendium of Neutron Spectra and Detector Responses for Radiation Protection Purposes, IAEA Technical Report Ser. No.318, IAEA, Vienna, 1990.
[43] T.E. Valentine, MCNP-DSP Users Manual, Oak Ridge National Laboratory, 2001. ORNL/TM-13334/2.
[44] J.C.G. Walker, Evolution of the Atmosphere, 1977.
[45] G.F. Knoll, Radiation Detection and Measurement, second ed., Wiley, New York, 1989.
[46] G. Mauri, F. Messi, K. Kanaki, R. Hall-Wilton, F. Piscitelli, Fast neutron sensitivity for ^{3}He detectors and comparison with Boron-10 based neutron detectors, EPJ Tech. Instrum. 6 (2019) 3.
[47] F. Piscitelli, G. Mauri, A. Laloni, R. Hall-Wilton, Verification of He-3 proportional counters' fast neutron sensitivity through a comparison with He-4 detectors He-3 and He-4 proportional counters' fast neutron sensitivity and evaluation of the cosmic neutron fluxes at ESS, Eur. Phys. J. Plus 135 (2020) 577.
[48] ISO 230-7, Test Code for Machine Tools-Part7: Geometric Accuracy of Axes of Rotation, 2015.
[49] S. Ghosh, A. Sharma, G. Talukder, Zirconium: an abnormal trace element in biology, Biol. Trace Elem. Res. 35 (1992) 247–271.
[50] M. Tanveer, L. Wang, Potential targets to reduce beryllium toxicity in plants: a review, Plant Physiol. Biochem. 139 (2019) 691–696.
[51] Shanghai metals market (SMM), November. https://www.metal.com/, 2021.
[52] K.J.R. Rosman, P.D.P. Taylor, IUPAC subcommittee for isotopic abundance measurements, Pure Appl. Chem. 71 (1999) 1593–1607.
[53] M.J. Fayer, G.W. Gee, Neutron Scattering, Encyclopedia of Soils in the Environment, 2005, pp. 6–12.
[54] E.L. Greacen, G. Schrale, The effect of bulk density on neutron meter calibration, Aust. J. Soil Res. 14 (1976) 159–169.
[55] P.G. Marais, W.B.D.E.V. Smit, Effect of bulk density and of hydrogen in forms other than free water on the calibration curve of the neutron moisture meter, South Afr. J. Agric. Sci. 5 (1962) 225–238.
[56] E. Dian, K. Kanaki, R.J. Hall-Wilton, P. Zagyvai, Sz Czifrus, Neutron activation and prompt gamma intensity in Ar/CO_2-flled neutron detectors at the European Spallation Source, Appl. Radiat. Isot. 128 (2017) 275–786.
[57] M.M. Bournea, C. Mussi, E.C. Miller, S.D. Clarke, S.A. Pozzi, A. Gueorguiev, Characterization of the CLYC detector for neutron and photon detection, Nucl. Instrum. Methods Phys. Res. 736 (2014) 124–127.